









Chirality locking charge density waves in a chiral crystal

Geng Li ^{1,2,3,4,7}, Haitao Yang ^{1,2,7}, Peijie Jiang^{1,2,7}, Cong Wang ^{5,7}, Qiuzhen Cheng^{1,2}, Shangjie Tian ⁵, Guangyuan Han^{1,2}, Chengmin Shen^{1,2}, Xiao Lin^{1,2}, Hechang Lei ⁵✉, Wei Ji ⁵✉, Ziqiang Wang ⁶✉ & Hong-Jun Gao ^{1,2,3,4}✉

In Weyl semimetals, charge density wave (CDW) order can spontaneously break the chiral symmetry, gap out the Weyl nodes, and drive the material into the axion insulating phase. Investigations have however been limited since CDWs are rarely seen in Weyl semimetals. Here, using scanning tunneling microscopy/spectroscopy (STM/S), we report the discovery of a novel unidirectional CDW order on the (001) surface of chiral crystal CoSi - a unique Weyl semimetal with unconventional chiral fermions. The CDW is incommensurate with both lattice momentum and crystalline symmetry directions, and exhibits an intra unit cell π phase shift in the layer stacking direction. The tunneling spectrum shows a particle-hole asymmetric V-shaped energy gap around the Fermi level that modulates spatially with the CDW wave vector. Combined with first-principle calculations, we identify that the CDW is locked to the crystal chirality and is related by a mirror reflection between the two enantiomers of the chiral crystal. Our findings reveal a novel correlated topological quantum state in chiral CoSi crystals and raise the potential for exploring the unprecedented physical behaviors of unconventional chiral fermions.

¹Institute of Physics, Chinese Academy of Sciences, 100190 Beijing, China. ²School of Physical Sciences, University of Chinese Academy of Sciences, 100190 Beijing, China. ³CAS Center for Excellent in Topological Quantum Computation, University of Chinese Academy of Sciences, 100190 Beijing, China. ⁴Songshan Lake Materials Laboratory, Dongguan, Guangdong 523808, PR China. ⁵Beijing Key Laboratory of Optoelectronic Functional Materials & Micro-Nano Devices, Department of Physics, Renmin University of China, 100872 Beijing, PR China. ⁶Department of Physics, Boston College, Chestnut Hill, MA, USA. ⁷These authors contributed equally: Geng Li, Haitao Yang, Peijie Jiang, Cong Wang. ✉email: hlei@ruc.edu.cn; wji@ruc.edu.cn; wangzi@bc.edu; hjgao@iphy.ac.cn

CDW is an electronic state in conducting materials where the charge density is periodically modulated. Experimentally, the formation of CDW is usually accompanied by increase in resistivity^{1,2}, gap opening around Fermi level^{3–7}, periodic modulations of the density of states, and distortions of the lattice due to electron-phonon coupling^{3–5,8}. CDWs have been widely observed in crystals. In Weyl semimetals, the chiral Weyl fermions, with spin parallel to the momentum, are usually very stable, and CDW is rarely seen due to the low density of states at the Fermi level. There are several theoretical proposals for realizing CDWs in Weyl semimetals via chiral symmetry breaking^{9,10} and electron-electron interactions^{11,12}. Thus far, Weyl semimetals hosting CDWs are limited to very few quasi-dimensional materials^{1,13}.

CoSi is a diamagnetic^{14,15}, three-dimensional covalent compound in the chiral crystal family^{16–21} described by a cubic B20 structure with space group of P2₁3 (Fig. 1a). Its lattice structure has a well-defined handedness due to the lack of mirror and inversion symmetries²², enabling two different growth enantiomers (referred to as CoSi and SiCo). The band structure of CoSi hosts two novel types of symmetry-enforced chiral Weyl nodes, the spin-1 and charge-2 nodes^{14,23–29}, which are widely separated in momentum space. Long Fermi arcs connecting their surface projections have been observed by angle-resolved photoemission spectroscopy (ARPES) measurements from different groups^{24,25,29} and STM³⁰. We report the discovery of a correlated Weyl fermion state – an incommensurate CDW whose wave vector is locked to the chirality/handedness of CoSi and related by mirror reflection between the two distinct enantiomers.

Results

Uniaxial CDW on CoSi (001) surface. A typical STM topography on our samples shows the atomically resolved square lattice of the CoSi (001) surface with pronounced periodic stripe-

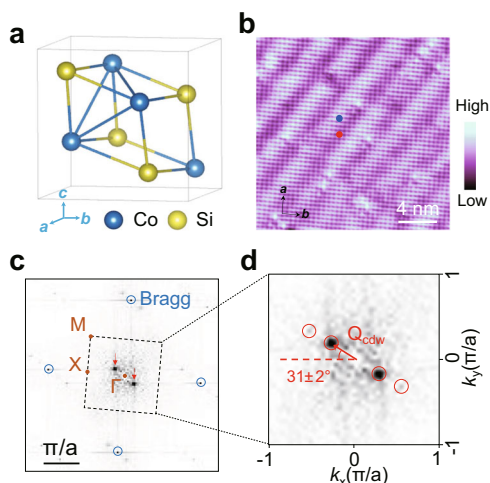


Fig. 1 Atomic structure, STM image and the FT images of the (001) surface of CoSi. **a** Crystalline structure of CoSi. **b** Large-scale STM image of CoSi (001) surface showing stripe-like modulations. The black arrows mark the crystalline symmetry directions. Scanning settings: $V_s = -200$ mV, $I_t = 0.4$ nA. **c** Fourier transformed image of **(b)**. The black dashed square outlines the 2D Brillouin zone of the surface. Bragg spots and high-symmetry points of the square lattice are outlined by blue circles and brown dots, respectively. Around the Γ point, two sharp peaks associated with the stripe modulation can be differentiated, as highlighted by red arrows. **d** Zoom-in image of the 2D Brillouin zone. The red arrow marks the CDW wave vector Q_{cdw} . The angle between Q_{cdw} and k_x direction is $31 \pm 2^\circ$.

like modulations (Fig. 1b). The crystalline symmetry directions are outlined by the black arrows. The square lattice of the Co atoms can be clearly resolved on the Co-terminated surface. Moreover, local defects appearing as bright or dark centers are observed. The existence of the defects are likely due to damage in crystal lattice during harsh surface treatment, which is required to obtain atomically flat CoSi (001) surface (see Methods). The drift-corrected Fourier transformed (FT) image (see Methods) in Fig. 1c shows, in addition to the atomic Bragg peaks, two sharp peaks (pointed to by red arrows) at the unidirectional wave vector Q_{cdw} corresponding to the stripe modulations. Zooming in to the first Brillouin zone (Fig. 1d), the magnitude of Q_{cdw} is measured to be $0.32 \pm 0.01 \pi/a$, while the angle between Q_{cdw} and k_x direction is $31 \pm 2^\circ$. As a result, the unidirectional charge modulations are incommensurate with both the lattice momentum and the high-symmetry lattice directions.

Electronic structure of the uniaxial CDW. The tunneling conductance dI/dV (r, V) maps are subsequently measured. The dI/dV map in Fig. 2a acquired at $V = -6$ mV shows clearly the unidirectional stripe modulations. The corresponding Fourier transform (Fig. 2b) exhibits the same Q_{cdw} as obtained from the topography. To confirm that the stripe modulations correspond to an electronic order such as the CDW, we took dI/dV maps at different energies (see Supplementary Fig. 1) and obtain the drift-corrected FT images from -30 to 30 mV. The normalized intensity of the FT along the blue dashed arrow in Fig. 2b is shown as a function of bias in Fig. 2c. Clearly, the wave vector of the stripe modulation is nondispersive and peaks around Q_{cdw} at all energies. The higher harmonic of the modulation is also visible in Fig. 2c. This is in contrast to the energy dispersive quasiparticle interference patterns (QPI) due to the bulk or surface Fermi arc states (Supplementary Fig. 2), and suggests the stripe modulations originate from unidirectional charge order.

Further evidence for charge modulation can be seen by comparing the dI/dV maps between the occupied and unoccupied states. In Fig. 2d, the dI/dV maps taken at 24 mV (upper panel) and -24 mV (lower panel) show stripe modulations with a clear contrast reversal³, as highlighted by the red and black dashed lines. This intensity reversal is consistent with the formation of a unidirectional Peierls CDW, where enhanced conductance for tunneling out of occupied states at a $V < 0$ in the region with charge accumulation implies enhanced conductance of a similar amplitude for tunneling into unoccupied state around $-V$ over the region with charge depletion. Throughout the measurements, our data always exhibit such a contrast reversal between filled and empty states, which provide key evidence for the formation of a unidirectional CDW. We note that the CDW stripes are relatively vague in the dI/dV maps (Fig. 2a, d) since the local density of states are easily affected by surface defects which are introduced during sample preparation (see Methods). However, strong and ordered CDW stripes can be observed in the topographic images at the same regions (Supplementary Fig. 3).

To probe the impact of the incipient CDW on the low-energy electronic states, the typical dI/dV spectra, obtained at the positions on (blue) and off (red) the stripes as marked in Fig. 1b, is plotted in Fig. 2e. The overall density of states (DOS) profiles are similar and show pronounced and broad peaks around -100 mV and 82 mV, suggesting high density of dispersive electronic states around these energies. The predicted chiral Fermi arc states on the (001) surface by density functional theory (DFT) span this energy range^{14,31}, as confirmed by ARPES^{24,25,29}, and are likely to contribute to these broad spectral peaks. The DOS decreases below these energies toward the Fermi level, in good agreement with the Weyl semimetallic nature of CoSi¹⁴. Remarkably, a

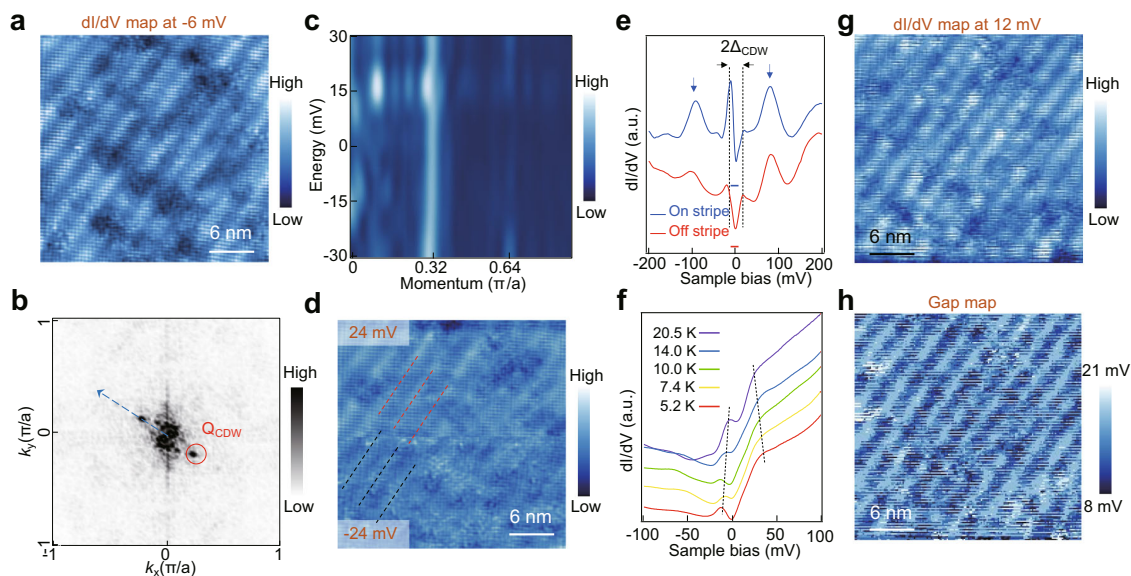


Fig. 2 Charge density wave on the (001) surface of CoSi. **a** dI/dV map of a surface region with the stripe modulation taken under -6 mV. **b** 2D Brillouin zone of the surface withdrawn from the FT image of (**a**). The CDW spot is outlined by a red circle. **c** Normalized intensity profiles of the FT images along the blue dashed arrow in (**b**) under bias voltages from -30 mV to 30 mV. The intensity peaks around Q_{CDW} under different energies. The CDW wave vector is nondispersive with energy. **d** dI/dV maps of the region in (**a**) taken at 24 mV (upper panel) and -24 mV (lower panel). The bright stripes of the upper (lower) are outlined by red (black) dashed lines. **e** Typical dI/dV curves taken on (blue) and off (red) the bright stripes in Fig. 1b. Zero conductance for each spectrum is marked with a solid horizontal line. The blue arrows indicate two broad peaks in the spectra. The CDW gap $2\Delta_{CDW}$ is determined by the energy spacing between the left and right coherence peaks. **f** Temperature dependence of the CDW gap. The dI/dV spectra are taken at a region different from that in Fig. 1b. Each curve is averaged from 10 independent dI/dV spectrum on the same bright stripe under different temperatures. The gap size gradually decreases with increasing temperature. **g** dI/dV map at 12 mV. **h** Gap map of the region in (**g**) acquired by recording the gap sizes at each pixel, showing a modulation of gap size by the CDW stripes.

particle-hole asymmetric energy gap emerges at low energies together with two sharp peaks at the gap edges and a V-shaped in-gap DOS having the minimum located near the Fermi level (Fig. 2e). Note that the energy gap is significantly larger than the spin-orbit coupling (SOC) induced band splitting^{29,30}, which has been observed to be less than 2 meV^{32–34}. We thus speculate that the spectral gap around E_F is the CDW gap due to the incommensurate charge modulation. Extracting the gap size from the peak to peak distance (Fig. 2e), we obtain $2\Delta_{cdw} \approx 29$ meV. We note that the gap size ($2\Delta_{cdw}$) varies from 12 to 40 meV in different regions of three CoSi(001) samples.

Additional evidence supporting an incommensurate CDW gap in the DOS comes from the temperature dependence of the differential conductance. Figure 2f displays the temperature evolution of the asymmetric dI/dV curves obtained at an on-stripe location, showing a gradual reduction of the CDW gap size with increasing temperature³⁵. Our STM/S can clearly reveal stripe modulations up to 80 K (Supplementary Fig. 4). To gain insights into the melting temperature of the charge modulations, we performed low energy electron diffraction (LEED) measurements, which provide an estimate of the CDW transition temperature ~ 150 K (Supplementary Fig. 5).

The definitive evidence for the causal relations between the gap in the DOS spectrum and the unidirectional spatial modulations requires the spatial variations of the spectral gap. To this end, the dI/dV map at $V = 12$ mV is shown in Fig. 2g. Extracting the gap value from the local tunneling spectrum at every point (Fig. 2g), we produce the gap map $2\Delta_{cdw}(r)$ shown in Fig. 2h. Intriguingly, the gap sizes exhibit the same spatial modulations matching those of the striped modulations in the dI/dV map and the topography, confirming the unidirectional CDW nature of the spatial modulations and the low-energy V-shaped gap in the DOS.

Unconventional properties of the CDW across steps. We next demonstrate the unconventional properties of the unidirectional CDW, which manifest most remarkably across the step edges. We observe two types of terraces due to the absence of inversion symmetry³⁰. The topmost atoms on different types of terraces can only overlap after a glide-mirror symmetry operation (Fig. 3a, b, Supplementary Fig. 6). The same type of terraces are connected by steps with heights of integer times the c -axis lattice constant c (even steps), while two terraces of different types are connected by step heights of half odd integer times c (odd steps). Such odd steps have been reported to play important roles in modifying the midgap step edge states in a topological crystalline insulator³⁶. Hereafter we refer to the two types of terraces as terraces with different indices (n or $n + 1/2$) (Fig. 3b). Figure 3a shows a region with multiple terraces. The success step height between adjacent terraces is measured to be ~ 2.3 Å, about half of the c -axis lattice constant. Interestingly, the CDW stripes are in phase across even steps (Fig. 3c, d), while they are out of phase across odd steps (Fig. 3e, f). The in phase (out of phase) CDW pattern across even (odd) steps is reproducible in different CoSi samples. The near π phase shift across odd steps suggests strong inhomogeneous intra-unit cell charge distribution (Fig. 3e, f) with intricate correlations along the c -direction. This is consistent with the atomically resolved dI/dV linecut showing strong intra-unit cell conductance modulations (Supplementary Figs. 7 and 8).

Surprisingly, the dI/dV line shape associated with the CDW gap shows intriguing spatial evolution across an odd step (Fig. 3g–i). On the lower terrace in Fig. 3g, the asymmetric DOS has a larger spectral weight at the coherence peak on the unoccupied side at positive bias. This asymmetry reverses on the upper terrace, with higher spectral weight for coherence peak on the occupied side at negative bias. This reversal of line shape

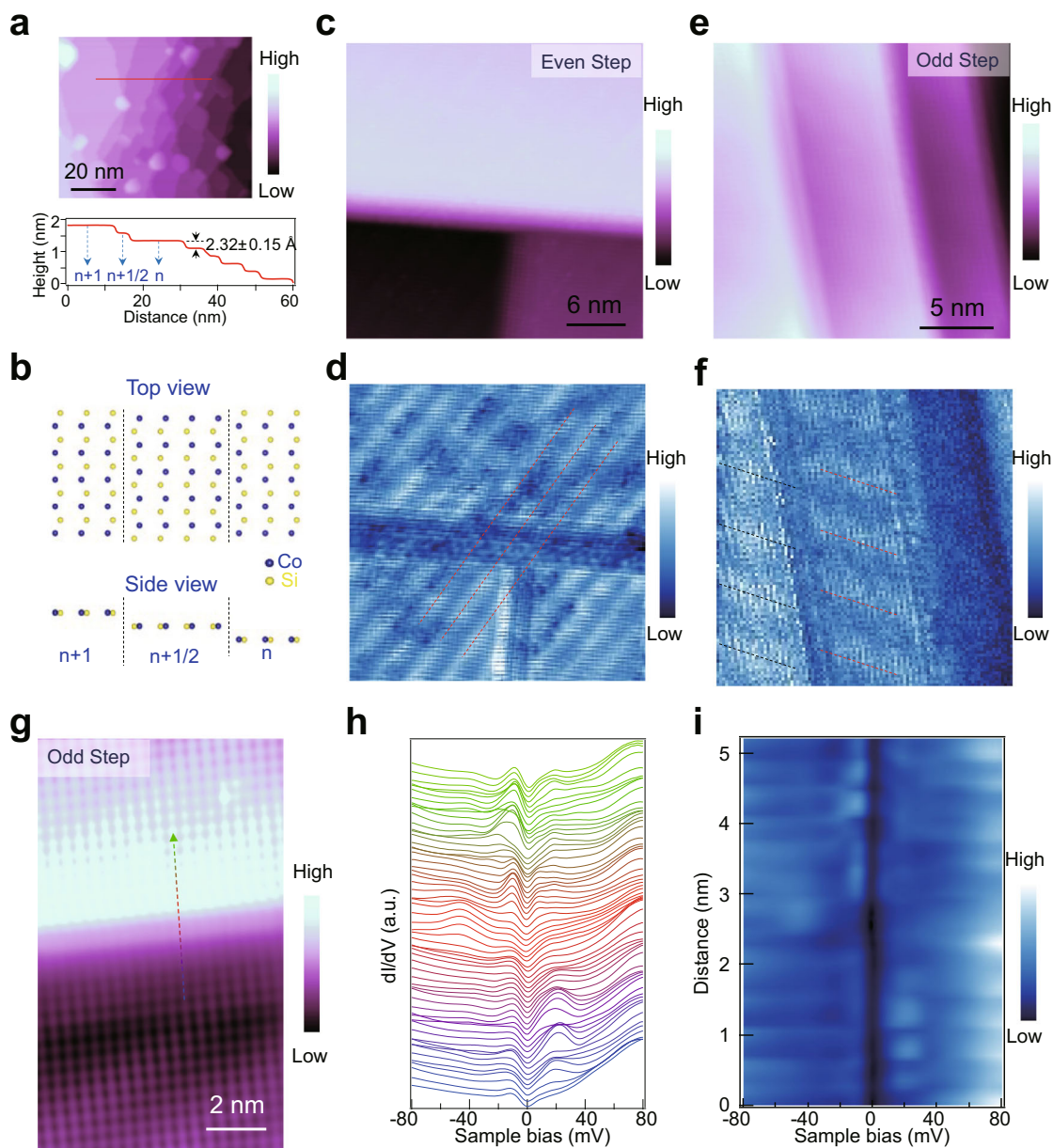


Fig. 3 Spatial evolution of CDW pattern and dI/dV spectra across steps. **a** Upper panel, a surface region showing terraces with different indices. Scanning settings: $V_s = -1$ V, $I_t = 0.6$ nA. Lower panel, height profile along the red line in the upper panel, showing sequential steps with half of the lattice constant along c axis. **b** Schematic drawing of the atomic arrangement of the terraces. The surface atoms on terraces possess n and $n + 1/2$ indices, and are linked with glide-mirror symmetry. STM image (**c**) and dI/dV map under zero bias (**d**) of a region with steps. The height difference between the highest (upper part in (**c**)) and lowest (lower left part in (**c**)) terraces is 2 times of the c -axis lattice constant c . The CDW stripes are in phase across even steps, as outlined by red dashed lines. Scanning settings of **c**: $V_s = -200$ mV, $I_t = 0.1$ nA. STM image (**e**) and dI/dV map under zero bias (**f**) of a region with sequential odd steps with heights of $2.5c$. The CDW stripes are out of phase across odd steps, as outlined by red and black dashed lines. Scanning settings of (**e**): $V_s = -200$ mV, $I_t = 0.1$ nA. **g** STM image of an odd step. Scanning settings: $V_s = 500$ mV, $I_t = 0.1$ nA. **h**, **i**, Waterfall plot and intensity map of dI/dV spectra along the dashed arrow in (**g**). On the lower terrace, the asymmetric CDW coherence peaks show larger spectral weight under positive bias, while under negative bias the spectral weight of the coherence peak gets stronger on the upper terrace. This asymmetry reverses across the odd step.

asymmetry is absent across even steps, where only modulations of the CDW gap size is observed (Supplementary Fig. 9). To the best of our knowledge, this behavior has not been observed in other CDW systems. Similar to chiral crystal PdGa, another member of the space group $P2_13$, the terraces across an odd step belong to the same enantiomer^{17,37}. The reversal of the asymmetry associated with the spectral weight transfer is closely related to the phase shift of CDW across odd steps, where the CDW order parameter picks up an additional π phase (Fig. 3e, f).

Discussion

We next turn to the implication and the possible origin of the incommensurate unidirectional CDW in CoSi. Two recent transport studies have shown the existence of phonon-drag effect in CoSi^{32,38}, providing experimental evidence for significant electron-phonon interactions. The CDW can also be induced by electron-electron interactions when a large density of states is present due to partial Fermi surface nesting. In $(\text{TaSe}_4)_2\text{I}$, where similar CDW patterns have been recently observed³⁹, there are 24 pairs of Weyl points present around the Fermi energy. A linear

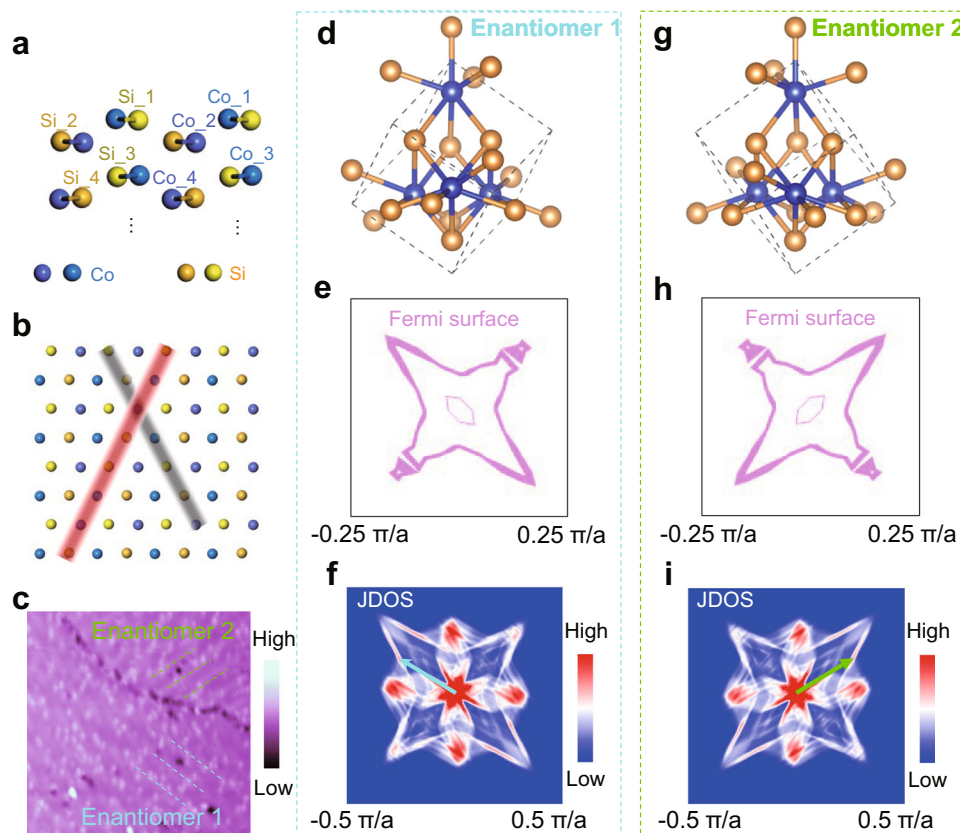


Fig. 4 Origin of chirality-locking, unidirectional CDW in CoSi. **a** Atomic structure of the four sub-layers in a unit cell of CoSi. **b** Top view of the first and second sublayers. The red line outlines the electron hopping path of Co₁-Co₂-Si₂-Si₁-Co₁-Co₂.... The gray line outlines another path following the same atomic sequence in the two-sublayer model. These two paths are inequivalent with each other in bulk CoSi. **c** Large-scale STM image showing coexistence of two different crystal enantiomers separated by a domain boundary. The blue and green dashed lines highlight the CDW stripes of enantiomers 1 and 2, respectively. The CDW orders are unidirectional in both enantiomers, but their CDW wave vectors point to different directions respectively. Atomic structures of crystal enantiomers 1 (**d**) and 2 (**g**). DFT revealed constant-energy contours of the Fermi surface at the adjusted Fermi level of enantiomers 1 (**e**) and 2 (**h**). These contours are only distributed around the Γ point in the k -space and the CDW was observed on the x - y plane of the crystal, thus, a slab at $k_z = 0$ with a range of $\pm 0.25 \pi/a$ was plotted. Derived JDOS plots, with numerically enhanced contrast, of the DFT Fermi surface contours of enantiomers 1 (**f**) and 2 (**i**). The blue (**f**) and green (**i**) arrows mark the experimentally observed CDW wave vectors in both direction and amplitude for enantiomers 1 and 2, respectively. The atomic structures, energy contours and JDOS of the two enantiomers show mirror symmetry with each other.

combination of different nesting vectors has been argued to give rise to the experimentally observed short CDW wave vector⁴⁰. The chiral crystal CoSi, on the other hand, has only one pair of well-separated Weyl nodes at Γ and R in the 3D Brillouin zone¹⁴, and their spanning vector is far off in both magnitude and direction from the observed incommensurate CDW wave vector. As a result, if near nesting conditions are at play, the observed CDW is to originate from the individual small Fermi surfaces around the zone center and zone corners¹⁴.

Further insights arise upon a closer examination of CDW direction with respect to the unique chiral crystal structure of CoSi. In each unit cell, the Co and Si atoms are distributed in four sublayers, labeled as 1 to 4 in Fig. 4a. The interlayer spacing between the top two sublayers is 80 pm, while the 2nd and 3rd sublayers are separated by a larger spacing of 131 pm. The observed stripes are oriented along path Co₁-Co₂-Si₂-Si₁-Co₁-Co₂..., as indicated by the red line in the top view of sublayers 1 and 2 in Fig. 4b, involving inter-sublayer tunneling. The other path highlighted by the gray line in Fig. 4b is inequivalent due to the absence of mirror and rotation symmetries associated with the chiral handedness of the crystal, when sublayers 3 and 4 are taken into account (Supplementary Fig. 10). This gives rise to the uniaxial behavior of the CDW, which is consistent with the absence of electronic stripe

domains with the other orientation over structurally well-defined regions.

Occasionally, we observe a structural domain boundary on the surface, separating the observed area into two regions with different enantiomers (Fig. 4c). While the two regions share the same high-symmetry lattice directions, the orientations of the CDW wave vectors are remarkably different, as outlined by the blue and green dashed lines. The angle between those two CDW wave vectors in the two chiral structural enantiomers is $\sim 69^\circ$ (Supplementary Fig. 11), pointing to that the CDW is locked to the chiral handedness of the crystal enantiomers and the two regions can be transformed to each other by a mirror symmetry operation.

To develop more microscopic understanding of the chirality locking CDW wave vector in relation to the handedness of the CoSi crystal, we performed DFT calculations for the two different enantiomers (Fig. 4d, g). The corresponding electronic structures (Supplementary Fig. 12) show a flat band at the Γ point lying 15 meV above the Fermi level²⁹. In real materials, this flat band has been observed by ARPES measurements to lie about 5 meV below the Fermi level^{24,29}, possibly due to electron correlation and/or internal electron doping effects. We therefore plot the two sets of constant energy contours at 15 meV above the calculated Fermi level in the 2D Brillouin zone, and regard them as the

approximate “adjusted” Fermi surfaces for the two enantiomers (Fig. 4e, h). Each set of contours contains four lobes, and the two sets are related by mirror reflection. This is likely the reason behind the observed uniaxial electronic behavior. The joint density of states (JDOS) of the corresponding Fermi surface contours were calculated and plotted in Fig. 4f, i for both crystal enantiomers. Remarkably, the measured incommensurate CDW wave vectors, superimposed using the blue and green arrows, match unique sections of the JDOS with enhanced intensity for both enantiomers related by mirror symmetry. We also calculated the phonon dispersion of bulk CoSi and the result shows weak electron phonon coupling (Supplementary Fig. 13). While more theoretical and experimental investigations are desirable to probe the microscopic origin, these results pointing to an electronic structure of CoSi harboring high density of quasiparticle scatterings at these wave vectors, making it conceivable that electronic correlations can drive the observed unconventional incommensurate CDW.

The combined STM experiments and DFT analysis suggest that the chirality locking CDW, with the sizable energy gap capable of reaching the Weyl node at Γ point below the Fermi level, has the potential to produce a mass gap for the unconventional chiral fermions. This raises the hope for realizing a highly nontrivial correlation-driven topological state.

Methods

Single-crystal growth and surface treatment. The quality of the sample surface has large influence on the clear observation of the CDW stripes. In order to obtain large and clean surface with atomically sharp steps, CoSi single crystal with good quality and sophisticated surface treatment is needed.

High-quality CoSi single crystals were synthesized by a chemical vapor transport method using I_2 as transport agent. High-purity Co powder (99.999%) and Si powder (99.99%) in 1:1 molar ratio were mixed with 150 mg I_2 and sealed in an evacuated quartz tube with a length of 110 mm and an inner diameter of 18 mm. The temperatures were set to 1000 °C (source side) and 900 °C (growth side), and kept for about 10 days, after which shiny single crystals (about 2 mm in size) with well-defined faces were obtained.

The crystal was then carefully grinded and polished along different high-symmetry orientations with different diamond lapping paper and polishing fluids by ALLIED™ MultiPrep polishing system. The desired crystal surface became shiny and showed no sign of scratches at 1000× optic magnification.

In order to minimize the chemical contamination on the surface, epoxy-free method was applied to mount the CoSi sample onto the STM sample holder. Sputtering and annealing procedure was carried out in an ultra-high vacuum chamber (base pressure better than 1×10^{-9} torr), connected with STM chamber. After transferred into the vacuum chamber, the sample was repeatedly sputtered and annealed under 950 K. More than 50 cycles of sputtering and annealing had been applied for each sample to guarantee smooth and clean terraces with atomically sharp steps, which is crucial for the observation of the CDW order.

STM/S experiments. The STM/S measurements were operated at different temperatures in an ultra-low temperature STM system. Tungsten tips were etched chemically and calibrated on Au(111) surface before use. The dI/dV spectra and maps were obtained by a standard lock-in technique with a modulation voltage of 0.3 mV at 973.0 Hz. All the images and dI/dV maps were taken under 280 mK unless specifically mentioned. To eliminate the STM tip-drift effect during long-time measurement in acquiring the topography and dI/dV maps, we apply the well-established Lawler-Fujita algorithm⁴¹ and obtain a set of displacement fields and drift-corrected topography. The displacement fields are then applied to the dI/dV maps acquired simultaneously with the topography.

DFT calculations. The DFT calculations were performed using the Perdew-Burke-Ernzerhof-generalized gradient approximation⁴² (PBE) for the exchange-correlation potential, the projector augmented wave method⁴³ and a plane-wave basis set as implemented in the Vienna ab-initio simulation package⁴⁴ (VASP). A kinetic energy cutoff of 700 eV for the plane wave basis set was used for structural relaxation and electronic structures calculations. A k-mesh of $20 \times 20 \times 20$ was adopted to sample the first Brillouin zone of the primitive unit cell of bulk CoSi. The shape and volume of each supercell were fully optimized and all atoms in the supercell were allowed to relax until the residual force per atom was less than 1×10^{-3} eV·Å⁻¹. The theoretical lattice constant of the bulk cubic crystal was 4.43 Å, well consistent with the experimental values. Electronic bandstructures were calculated with considering SOC based on the two distinct enantiomers. The constant energy contours in the 2D Brillouin zone ($k_z = 0$) were plotted at 15 meV above the

calculated Fermi level with an energy broadening of ± 1 meV. The JDOS of corresponding constant energy contours were derived using Fourier transformations.

Data availability

The data in this study are available from the corresponding authors on reasonable request.

Received: 24 December 2021; Accepted: 5 May 2022;

Published online: 25 May 2022

References

- Gooth, J. et al. Axionic charge-density wave in the Weyl semimetal (TaSe₄)₂ I. *Nature* **575**, 315–319 (2019).
- Tang, F. et al. Three-dimensional quantum Hall effect and metal-insulator transition in ZrTe₅. *Nature* **569**, 537–541 (2019).
- Barja, S. et al. Charge density wave order in 1D mirror twin boundaries of single-layer MoSe₂. *Nat. Phys.* **12**, 751–756 (2016).
- Gao, S. et al. Atomic-scale strain manipulation of a charge density wave. *Proc. Natl. Acad. Sci. USA* **115**, 6986–6990 (2018).
- Soumyanarayanan, A. et al. Quantum phase transition from triangular to stripe charge order in NbSe₂. *P. Natl. Acad. Sci. USA* **110**, 1623–1627 (2013).
- Ugeda, M. M. et al. Characterization of collective ground states in single-layer NbSe₂. *Nat. Phys.* **12**, 92–97 (2016).
- Yang, X. et al. Possible phason-polaron effect on purely one-dimensional charge order of Mo₆Se₆ nanowires. *Phys. Rev. X* **10**, 031061 (2020).
- Zong, A. et al. Evidence for topological defects in a photoinduced phase transition. *Nat. Phys.* **15**, 27–31 (2019).
- Wang, Z. & Zhang, S. C. Chiral anomaly, charge density waves, and axion strings from Weyl semimetals. *Phys. Rev. B* **87**, 161107 (2013).
- You, Y. Z., Cho, G. Y. & Hughes, T. L. Response properties of axion insulators and Weyl semimetals driven by screw dislocations and dynamical axion strings. *Phys. Rev. B* **94**, 085102 (2016).
- Roy, B. & Sau, J. D. Magnetic catalysis and axionic charge density wave in Weyl semimetals. *Phys. Rev. B* **92**, 125141 (2015).
- Laubach, M. et al. Density wave instabilities and surface state evolution in interacting Weyl semimetals. *Phys. Rev. B* **94**, 241102 (2016).
- Zhang, X. et al. Eightfold fermionic excitation in a charge density wave compound. *Phys. Rev. B* **102**, 035125 (2020).
- Tang, P. Z., Zhou, Q. & Zhang, S. C. Multiple types of topological fermions in transition metal silicides. *Phys. Rev. Lett.* **119**, 206402 (2017).
- Balasubramanian, B. et al. Chiral magnetism and high-temperature skyrmions in B20-ordered Co-Si. *Phys. Rev. Lett.* **124**, 057201 (2020).
- Chang, G. et al. Unconventional chiral fermions and large topological fermi arcs in RhSi. *Phys. Rev. Lett.* **119**, 206401 (2017).
- Schroter, N. B. M. et al. Observation and control of maximal Chern numbers in a chiral topological semimetal. *Science* **369**, 179–183 (2020).
- Li, H. et al. Chiral fermion reversal in chiral crystals. *Nat. Commun.* **10**, 5505 (2019).
- Schroter, N. B. M. et al. Chiral topological semimetal with multifold band crossings and long Fermi arcs. *Nat. Phys.* **15**, 759–765 (2019).
- Xu, S. et al. Quantum oscillations and electronic structure in the large-Chern number semimetal RhSn. *Phys. Rev. B* **100**, 245146 (2019).
- Wilde, M. A. et al. Symmetry-enforced topological nodal planes at the Fermi surface of a chiral magnet. *Nature* **594**, 374–379 (2021).
- Ni, Z. L. et al. Giant topological longitudinal circular photo-galvanic effect in the chiral multifold semimetal CoSi. *Nat. Commun.* **12**, 154 (2021).
- Hasan, M. Z. et al. Weyl, Dirac and high-fold chiral fermions in topological quantum matter. *Nat. Rev. Mater.* **6**, 784–803 (2021).
- Rao, Z. C. et al. Observation of unconventional chiral fermions with long Fermi arcs in CoSi. *Nature* **567**, 496–499 (2019).
- Sanchez, D. S. et al. Topological chiral crystals with helicoid-arc quantum states. *Nature* **567**, 500–505 (2019).
- Sanchez, D. S. et al. Helicoid-arc van Hove singularities in topological chiral crystals. *arXiv:2108.13957* (2021).
- Xu, B. et al. Optical signatures of multifold fermions in the chiral topological semimetal CoSi. *P. Natl. Acad. Sci. USA* **117**, 27104–27110 (2020).
- Tang, K. et al. Spin Hall effect in a spin-1 chiral semimetal. *Phys. Rev. Res.* **3**, 033101 (2021).
- Takane, D. et al. Observation of Chiral Fermions with a Large Topological Charge and Associated Fermi-Arc Surface States in CoSi. *Phys. Rev. Lett.* **122**, 076402 (2019).
- Yuan, Q. Q. et al. Quasiparticle interference evidence of the topological Fermi arc states in chiral fermionic semimetal CoSi. *Sci. Adv.* **5**, eaaw9485 (2019).

31. Pshenay-Severin, D. A., Ivanov, Y. V., Burkov, A. A. & Burkov, A. T. Band structure and unconventional electronic topology of CoSi. *J. Phys.: Condens. Matter* **30**, 135501 (2018).
32. Xu, X. T. et al. Crystal growth and quantum oscillations in the topological chiral semimetal CoSi. *Phys. Rev. B* **100**, 045104 (2019).
33. Wu, D. S. et al. Single crystal growth and magnetoresistivity of topological semimetal CoSi. *Chin. Phys. Lett.* **36**, 077102 (2019).
34. Wang, H. et al. de Haas-van Alphen quantum oscillations and electronic structure in the large-Chern-number topological chiral semimetal CoSi. *Phys. Rev. B* **102**, 115129 (2020).
35. Borisenko, S. V. et al. Pseudogap and charge density waves in two dimensions. *Phys. Rev. Lett.* **100**, 196402 (2008).
36. Sessi, P. et al. Robust spin-polarized midgap states at step edges of topological crystalline insulators. *Science* **354**, 1269–1273 (2016).
37. Sessi, P. et al. Handedness-dependent quasiparticle interference in the two enantiomers of the topological chiral semimetal PdGa. *Nat. Commun.* **11**, 3507 (2020).
38. Schnatmann, L. et al. Signatures of a charge density wave phase and the chiral anomaly in the fermionic material cobalt monosilicide CoSi. *Adv. Electron. Mater.* **6**, 1900857 (2020).
39. Yi, H. M. et al. Surface charge induced Dirac band splitting in a charge density wave material (TaSe₄)₂I. *Phys. Rev. Res.* **3**, 013271 (2021).
40. Shi, W. J. et al. A charge-density-wave topological semimetal. *Nat. Phys.* **17**, 381 (2021).
41. Lawler, M. J. et al. Intra-unit-cell electronic nematicity of the high-T_c copper-oxide pseudogap states. *Nature* **466**, 347–351 (2010).
42. Perdew, J. P., Burke, K. & Ernzerhof, M. Generalized gradient approximation made simple. *Phys. Rev. Lett.* **77**, 3865–3868 (1996).
43. Kresse, G. & Joubert, D. From ultrasoft pseudopotentials to the projector augmented-wave method. *Phys. Rev. B* **59**, 1758–1775 (1999).
44. Kresse, G. & Furthmüller, J. Efficiency of ab-initio total energy calculations for metals and semiconductors using a plane-wave basis set. *Comp. Mater. Sci.* **6**, 15–50 (1996).

Acknowledgements

This work is supported by the Ministry of Science and Technology of China (2019YFA0308500, 2018YFA0305700 and 2018YFE0202600), the National Natural Science Foundation of China (61888102, 51991340, 52072401, 61761166009 and 11974422), the Chinese Academy of Sciences (XDB28000000, XDB07000000, XDB30000000, and YSBR-003), and Beijing Natural Science Foundation (Grant No. Z200005). Z.W. is supported by the US DOE, Basic Energy Sciences Grant No. DE-FG02-99ER45747. Calculations were performed at the Physics Lab of High-Performance Computing of Renmin University of China, Shanghai Supercomputer Center.

Author contributions

H.-J.G. and G.L. designed the experiments; H.Y., Q.C., S.T., and H.L. synthesized the CoSi single crystals and polished the surfaces; G.L., P.J., G.H. and X.L. performed the STM/S experiment; G.L. performed the LEED experiment; C.W. and W. J. performed the DFT calculations; G.L., P.J., C.S., W.J., Z.W., and H.-J.G. analyzed the experimental data with inputs from all other authors; G.L., P.J., and G.H. plotted the figures. G.L., W.J., Z.W., and H.-J.G. wrote the manuscript with input from all other authors. H.-J.G. and Z.W. supervised the project.

Competing interests

The authors declare no competing interests.

Additional information

Supplementary information The online version contains supplementary material available at <https://doi.org/10.1038/s41467-022-30612-0>.

Correspondence and requests for materials should be addressed to Hechang Lei, Wei Ji, Ziqiang Wang or Hong-Jun Gao.

Peer review information *Nature Communications* thanks the anonymous, reviewer(s) for their contribution to the peer review of this work.

Reprints and permission information is available at <http://www.nature.com/reprints>

Publisher's note Springer Nature remains neutral with regard to jurisdictional claims in published maps and institutional affiliations.



Open Access This article is licensed under a Creative Commons Attribution 4.0 International License, which permits use, sharing, adaptation, distribution and reproduction in any medium or format, as long as you give appropriate credit to the original author(s) and the source, provide a link to the Creative Commons license, and indicate if changes were made. The images or other third party material in this article are included in the article's Creative Commons license, unless indicated otherwise in a credit line to the material. If material is not included in the article's Creative Commons license and your intended use is not permitted by statutory regulation or exceeds the permitted use, you will need to obtain permission directly from the copyright holder. To view a copy of this license, visit <http://creativecommons.org/licenses/by/4.0/>.

© The Author(s) 2022